

# Modelling and analysis of the distortion of strongly-coupled wireless power transfer systems with SS and LCC–LCC compensations

ISSN 1755-4535

Received on 8th June 2018

Revised 12th January 2019

Accepted on 28th January 2019

doi: 10.1049/iet-pel.2018.5542

www.ietdl.org

Yiming Zhang<sup>1</sup>, Zhengchao Yan<sup>1,2</sup>, Tianze Kan<sup>1</sup>, Yanding Liu<sup>3</sup>, Chunting Chris Mi<sup>1</sup> ✉

<sup>1</sup>Department of Electrical and Computer Engineering, San Diego State University, 5500 Campanile Drive E426A, San Diego, USA

<sup>2</sup>School of Marine Science and Technology, Northwestern Polytechnical University, 127 West Youyi Road, Xi'an, People's Republic of China

<sup>3</sup>Huawei Technologies Co., Ltd, Shenzhen, People's Republic of China

✉ E-mail: mi@ieee.org

**Abstract:** Accurate modelling is necessary for designing a wireless power transfer (WPT) system and currently, first harmonic approximation (FHA) is widely used. However, it is not accurate for WPT systems with a strong coupling, such as fast charging of electric vehicles with a coupling coefficient of 0.80, compared to the conventional wireless charging with a coupling coefficient of 0.15–0.30. This study develops accurate models for WPT systems with series–series (SS) and LCC–LCC compensations. For the SS compensation with a strong coupling, the transmitter and receiver currents are distorted, leading to much larger values than the estimations from FHA, which determines the selection of power switches and resonant capacitors. For the LCC–LCC compensation, the transmission coil currents are only highly distorted with rich third-order harmonics at the vicinity of the 0.889 coupling coefficient, leading to low efficiency and large coil current ratings. For the experimental prototype, the efficiency drop can be over 3%, which is significant, especially for high-power systems. The WPT system with the LCC–LCC compensation should avoid operation in the vicinity of this particular coupling coefficient. Furthermore, experiments are conducted, and the results perfectly match the calculations, demonstrating the accuracy of the proposed models.

## 1 Introduction

The application of wireless power transfer (WPT) ranges from low-power scenarios like consumer electronics [1] and implantable medical devices [2] to high-power scenarios like electric vehicles [3] and railway transit [4], achieving convenience, safety, maintenance freedom, and longevity of devices due to reduced sparks. Magnetic induction WPT, or inductive power transfer (IPT), has received the most extensive research and commercial penetration [5–8]. In IPT, compensations are necessarily added to increase the transfer efficiency and reduce the VA rating of the power converters. Currently, there are two popular compensation topologies, series–series (SS) and LCC–LCC compensations.

Accurate modelling and analysis of a WPT system are of great importance as it provides researchers with valuable information in designing the system. There are mainly three theories in analysing a WPT system: coupled mode theory (CMT), bandpass filter (BPF), and circuit theory (CT). CMT is an approach to describe the coupling of vibrational systems in space or in time, particularly in WPT for analysing the coupled resonators [9, 10], but it is not intuitive. In BPF, the WPT system is designed in the same way as a second-order BPF [11, 12]. Still, it is not intuitive and the electric quantities cannot be directly obtained. CT is employed more widely due to its intuitiveness and simpleness. Currently, first harmonic approximation (FHA) of CT is used, in which only the fundamental harmonics of the voltages and currents are considered [13–15]. In most cases, it is accurate when high-order harmonics are suppressed due to the frequency selection characteristic of the resonant circuits.

High-power wireless charging for electric vehicles is one of the hot topics in WPT. Normally the charging distance is very short to improve the transferred power level and efficiency, leading to a strong coupling coefficient over 0.7. Typical examples include 60 kW power transfer by Conductix-Wampfler at a distance of 40 mm and some wireless charging electric bus projects (Bus projects in Italy 2003 and Chattanooga Area Regional Transportation Authority (CARTA) in the USA 2011) [16]. With a strong

coupling, the WPT system may contain rich harmonics with distorted current waveforms, resulting in low efficiency, and FHA is no longer accurate. Currently, most references analyse the WPT system based on FHA. Safaei and Woronowicz [17] divided the SS compensation into four modes of operation and assessed the accuracy of FHA, but the efficiency has not been evaluated and the output characteristics need investigations. Deng *et al.* [18] mentioned the distortion of the LCC–LCC compensation, but it is not severe due to a weak coupling.

In this paper, the models of the WPT systems with the SS and LCC–LCC compensations based on differential equations (DEs) are proposed. It is demonstrated that the waveforms with the proposed modelling method perfectly matches the experimental ones. With the proposed modelling method, researchers can better understand the system, more accurately select components in designing the system and avoid operation in low-efficiency zones. The contributions of this paper are

- i. Developed the DEs and more accurate models for the WPT systems with the SS and LCC–LCC compensations.
- ii. Investigated the distortion of the SS compensation at different coupling coefficients and discovered that the SS compensation has distortions when the coupling is strong, the harmonic currents do not contribute to the power transfer, and the output characteristics at a strong coupling are the same as that with a weak coupling.
- iii. Investigated the distortion of the LCC–LCC compensation and discovered that the LCC–LCC compensation is only highly distorted at the vicinity of the 0.889 coupling coefficient with large third-order harmonics, leading to low efficiency and large transmission coil current ratings.
- iv. Compared the distortions of the SS and LCC–LCC compensations and demonstrated that the LCC–LCC compensation is a more suitable topology for a strongly-coupled WPT system.

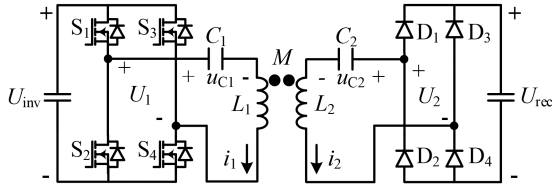


Fig. 1 Topology of a WPT system with SS compensation

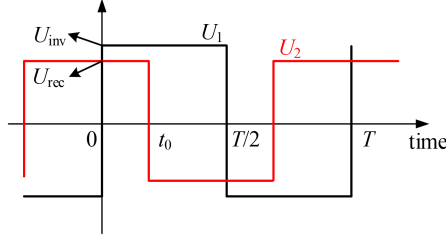


Fig. 2 AC voltage waveforms of inverter and rectifier

## 2 SS compensation

The SS compensation is the most popular choice for many wireless charging systems which is depicted in Fig. 1, where  $S_1$ – $S_4$  are the switches of the inverter,  $D_1$ – $D_4$  are the diodes of the rectifier,  $L_1$  ( $L_2$ ),  $C_1$  ( $C_2$ ),  $i_1$  ( $i_2$ ), and  $u_{C1}$  ( $u_{C2}$ ) are the inductance, the compensating capacitance, the current, and the capacitor voltage of the transmitter (receiver), respectively,  $M$  is the mutual inductance,  $U_{inv}$  is the inverter DC voltage,  $U_{rec}$  is the battery voltage, and  $U_1$  ( $U_2$ ) is the AC voltage of the inverter (rectifier).

For ease of analysis, assume that  $L_1 = L_2 = L_0$  and  $C_1 = C_2 = C_0$ . Thus,  $M = k \cdot L_0$ , where  $k$  is the coupling coefficient. The resonant frequency can be expressed as  $\omega_0 = 1/\sqrt{L_0 C_0}$

### 2.1 Model based on FHA

Based on FHA, only the fundamental harmonics of the AC voltages of the inverter and the rectifier are considered.  $U_1$  and  $U_2$  can be expressed as

$$U_1 = \frac{2\sqrt{2}}{\pi} U_{inv}, \quad U_2 = \frac{2\sqrt{2}}{\pi} U_{rec}. \quad (1)$$

At  $\omega_0$ , the root-mean-square (RMS) values of the transmitter and receiver currents are

$$I_1 = \frac{U_2}{\omega_0 M}, \quad I_2 = \frac{U_1}{\omega_0 M}. \quad (2)$$

Thus, the output power is

$$P_{trn} = \omega_0 M I_1 I_2 = \frac{U_1 U_2}{\omega_0 M}. \quad (3)$$

As can be seen from (2), the receiver current is mainly decided by the inverter DC voltage, making it a constant-current output characteristic. When the operating frequency equals

$$\omega_p = \frac{\omega_0}{\sqrt{1+k}}, \quad \omega_N = \frac{\omega_0}{\sqrt{1-k}}. \quad (4)$$

The WPT system with the SS compensation has a constant-voltage output characteristic [19].

### 2.2 Model based on DEs

FHA is inaccurate when the distortion cannot be ignored in the current waveforms. The waveforms of  $U_1$  and  $U_2$  are shown in Fig. 2. Since the waveforms are half-wave symmetrical, only the first half cycle is analysed. The results of the first half cycle can be easily extended to the second half cycle.  $t_0$  is the zero crossing

point of the receiver current, where  $U_2$  changes from positive to negative, and  $T$  is the period. During the stage  $[0, t_0]$ ,  $S_1$ ,  $S_4$ ,  $D_1$ , and  $D_4$  are on and the other switches are off; during the stage  $[t_0, T/2]$ ,  $S_1$ ,  $S_4$ ,  $D_2$ , and  $D_3$  are on and the other switches are off.

Take the inductor currents and capacitor voltages  $i_1$ ,  $i_2$ ,  $u_{C1}$ , and  $u_{C2}$  as the state variables, and the model in Fig. 1 for the stage  $[0, t_0]$  can be established by

$$\begin{cases} U_{inv} = u_{C1} + L_0 \frac{di_1}{dt} + kL_0 \frac{di_2}{dt}, & i_1 = C_0 \frac{du_{C1}}{dt} \\ U_{rec} = u_{C2} + L_0 \frac{di_2}{dt} + kL_0 \frac{di_1}{dt}, & i_2 = C_0 \frac{du_{C2}}{dt} \end{cases}. \quad (5)$$

By solving (5), the DEs for the inductor currents are

$$\begin{cases} (1+k)L_0 C_0 \frac{d^2(i_1+i_2)}{dt^2} + (i_1+i_2) = 0 \\ (1-k)L_0 C_0 \frac{d^2(i_1-i_2)}{dt^2} + (i_1-i_2) = 0 \end{cases}. \quad (6)$$

The characteristic roots for (6) are calculated as

$$\gamma_{1,2} = \pm j \frac{\omega_0}{\sqrt{1+k}}, \quad \gamma_{3,4} = \pm j \frac{\omega_0}{\sqrt{1-k}}. \quad (7)$$

The absolute value of the imaginary parts of (7) is the same as that in (4). The state variables in the stage  $[0, t_0]$  can be expressed as

$$\begin{cases} i_{1-1} = \frac{A_{1P}}{2} \sin(\omega_p t + B_{1P}) + \frac{A_{1N}}{2} \sin(\omega_N t + B_{1N}) \\ i_{2-1} = \frac{A_{1P}}{2} \sin(\omega_p t + B_{1P}) - \frac{A_{1N}}{2} \sin(\omega_N t + B_{1N}) \\ u_{C1-1} = U_{inv} - \frac{(1+k)\omega_p L_0}{2} A_{1P} \cos(\omega_p t + B_{1P}) \\ \quad - \frac{(1-k)\omega_N L_0}{2} A_{1N} \sin(\omega_N t + B_{1N}) \\ u_{C2-1} = U_{rec} - \frac{(1+k)\omega_p L_0}{2} A_{1P} \cos(\omega_p t + B_{1P}) \\ \quad + \frac{(1-k)\omega_N L_0}{2} A_{1N} \sin(\omega_N t + B_{1N}) \end{cases}, \quad (8)$$

where  $A_{1P}$ ,  $A_{1N}$ ,  $B_{1P}$ , and  $B_{1N}$  are the coefficients to be determined.

Similarly, the model in Fig. 1 for the stage  $[t_0, T/2]$  can be established by

$$\begin{cases} U_{inv} = u_{C1} + L_0 \frac{di_1}{dt} + kL_0 \frac{di_2}{dt}, & i_1 = C_0 \frac{du_{C1}}{dt} \\ -U_{rec} = u_{C2} + L_0 \frac{di_2}{dt} + kL_0 \frac{di_1}{dt}, & i_2 = C_0 \frac{du_{C2}}{dt} \end{cases}. \quad (9)$$

The DEs and the characteristic roots are the same as those of the first stage shown in (6) and (7). The state variables of the stage  $[t_0, T/2]$  can be expressed as

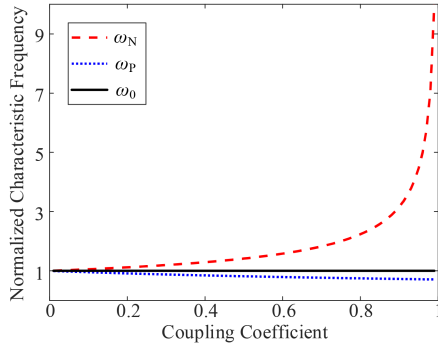


**Fig. 3** Characteristic frequencies varying with the coupling coefficient of the SS compensation

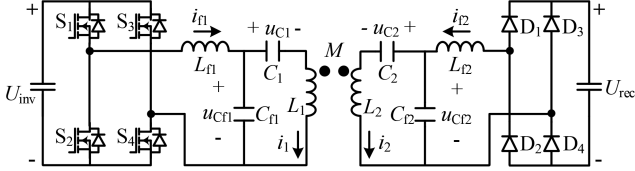


**Fig. 4** Topology of a WPT system with the LCC-LCC compensation

$$\left\{ \begin{array}{l} i_{1-2} = \frac{A_{2P}}{2} \sin(\omega_P t + B_{2P}) + \frac{A_{2N}}{2} \sin(\omega_N t + B_{2N}) \\ i_{2-2} = \frac{A_{2P}}{2} \sin(\omega_P t + B_{2P}) - \frac{A_{2N}}{2} \sin(\omega_N t + B_{2N}) \\ u_{C1-2} = U_{inv} - \frac{(1+k)\omega_P L_0}{2} A_{2P} \cos(\omega_P t + B_{2P}) \\ \quad - \frac{(1-k)\omega_N L_0}{2} A_{2N} \sin(\omega_N t + B_{2N}) \\ u_{C2-2} = -U_{rec} - \frac{(1+k)\omega_P L_0}{2} A_{2P} \cos(\omega_P t + B_{2P}) \\ \quad + \frac{(1-k)\omega_N L_0}{2} A_{2N} \sin(\omega_N t + B_{2N}) \end{array} \right. , \quad (10)$$

where  $A_{2P}$ ,  $A_{2N}$ ,  $B_{2P}$ , and  $B_{2N}$  are the coefficients to be determined.

To calculate the coefficients in (8) and (10), the initial conditions are

$$\left\{ \begin{array}{l} i_{1-1}(0) = -i_{1-2}\left(\frac{T}{2}\right), i_{1-1}(t_0) = i_{1-2}(t_0) \\ i_{2-1}(0) = -i_{2-2}\left(\frac{T}{2}\right), i_{2-1}(t_0) = i_{2-2}(t_0) \\ u_{C1-1}(0) = -u_{C1-2}\left(\frac{T}{2}\right), u_{C1-1}(t_0) = u_{C1-2}(t_0) \\ u_{C2-1}(0) = -u_{C2-2}\left(\frac{T}{2}\right), u_{C2-1}(t_0) = u_{C2-2}(t_0) \\ i_{2-1}(t_0) = 0. \end{array} \right. \quad (11)$$

Solving (11) yields

$$A_{1P} \sin B_{1P} = -\frac{U_{inv}}{(1+k)\omega_P L_0} \frac{\sin(\omega_P T/2)}{1 + \cos(\omega_P T/2)} + \frac{U_{rec}}{(1+k)\omega_P L_0} \frac{\sin \omega_P t_0 + \sin \omega_P (t_0 - (T/2))}{1 + \cos(\omega_P T/2)}, \quad (12)$$

$$A_{1P} \cos B_{1P} = \frac{U_{inv}}{(1+k)\omega_P L_0} - \frac{U_{rec}}{(1+k)\omega_P L_0} \frac{\cos \omega_P t_0 + \cos \omega_P (t_0 - (T/2))}{1 + \cos(\omega_P T/2)}, \quad (13)$$

$$A_{1N} \sin B_{1N} = -\frac{U_{inv}}{(1-k)\omega_N L_0} \frac{\sin(\omega_N T/2)}{1 + \cos(\omega_N T/2)} + \frac{U_{rec}}{(1-k)\omega_N L_0} \frac{\sin \omega_N t_0 + \sin \omega_N (t_0 - (T/2))}{1 + \cos(\omega_N T/2)}, \quad (14)$$

$$A_{1N} \cos B_{1N} = \frac{U_{inv}}{(1-k)\omega_N L_0} - \frac{U_{rec}}{(1-k)\omega_N L_0} \frac{\cos \omega_N t_0 + \cos \omega_N (t_0 - (T/2))}{1 + \cos(\omega_N T/2)}, \quad (15)$$

$$A_{2P} \sin B_{2P} = -\frac{U_{inv}}{(1+k)\omega_P L_0} \frac{\sin(\omega_P T/2)}{1 + \cos(\omega_P T/2)} + \frac{U_{rec}}{(1+k)\omega_P L_0} \frac{\sin \omega_P t_0 + \sin \omega_P (t_0 + (T/2))}{1 + \cos(\omega_P T/2)}, \quad (16)$$

$$A_{2P} \cos B_{2P} = \frac{U_{inv}}{(1+k)\omega_P L_0} - \frac{U_{rec}}{(1+k)\omega_P L_0} \frac{\cos \omega_P t_0 + \cos \omega_P (t_0 + (T/2))}{1 + \cos(\omega_P T/2)}, \quad (17)$$

$$A_{2N} \sin B_{2N} = -\frac{U_{inv}}{(1-k)\omega_N L_0} \frac{\sin(\omega_N T/2)}{1 + \cos(\omega_N T/2)} - \frac{U_{rec}}{(1-k)\omega_N L_0} \frac{\sin \omega_N t_0 + \sin \omega_N (t_0 + (T/2))}{1 + \cos(\omega_N T/2)}, \quad (18)$$

$$A_{2N} \cos B_{2N} = \frac{U_{inv}}{(1-k)\omega_N L_0} + \frac{U_{rec}}{(1-k)\omega_N L_0} \frac{\cos \omega_N t_0 + \cos \omega_N (t_0 + (T/2))}{1 + \cos(\omega_N T/2)}, \quad (19)$$

where  $t_0$  is unknown and can be calculated by letting  $i_{2-1}(t_0) = 0$ , which can be transformed into

$$A_{1P} \cos B_{1P} \sin \omega_P t_0 + A_{1P} \sin B_{1P} \cos \omega_P t_0 - A_{1N} \cos B_{1N} \sin \omega_N t_0 - A_{1N} \sin B_{1N} \cos \omega_N t_0 = 0. \quad (20)$$

By substituting (20) into (12)–(19),  $t_0$  can be derived. Thus, the equations for the coil currents and the capacitor voltages can be obtained. Note that the operating frequency not necessarily equals  $\omega_0$ . The period  $T$  should be changed according to different operating frequencies.

The two characteristic angular frequencies, which are the imaginary parts of (7), changing with the coupling coefficient  $k$  are plotted in Fig. 3. When  $k$  is small, these two characteristic frequencies are close to each other. With the increasing  $k$ , the difference between these two frequencies becomes more and more significant. It is the composition of these two distinctively different frequency components that leads to the distortion. According to (7), when  $k=0.889$ ,  $\gamma_{3,4}$  would triple the fundamental resonant angular frequency. Since the square wave of the inverter AC voltage has a large third harmonic component, the WPT system with the SS compensation at this particular coupling coefficient will have a large third harmonic current.

### 3 LCC-LCC compensation

The LCC-LCC compensation is another popular choice for the WPT systems, which is depicted in Fig. 4, where  $L_{f1}$  ( $L_{f2}$ ),  $C_{f1}$  ( $C_{f2}$ ),  $i_{f1}$  ( $i_{f2}$ ), and  $u_{Cf1}$  ( $u_{Cf2}$ ) are the compensation inductance, the parallel compensation capacitance, the compensation inductor current, and the parallel compensation capacitor voltage of the transmitter (receiver), respectively.

Similar to the SS compensation, assume that  $L_1 = L_2 = L_0$ ,  $C_1 = C_2 = C_0$ ,  $L_{f1} = L_{f2} = L_{f0}$ , and  $C_{f1} = C_{f2} = C_{f0}$ . Define  $\alpha = L_{f0}/L_0$ , and the resonant frequency can be expressed as

$$\omega_0 = \frac{1}{\sqrt{L_{f0}C_{f0}}} = \frac{1}{\sqrt{L_0 \frac{C_0 C_{f0}}{C_0 + C_{f0}}}}. \quad (21)$$

### 3.1 Model based on FHA

At  $\omega_0$ , the RMS values of the transmission and compensation coil currents can be calculated as

$$\begin{aligned} I_1 &= \frac{U_1}{\alpha \omega_0 L_0}, & I_2 &= \frac{U_2}{\alpha \omega_0 L_0}, \\ I_{f1} &= \frac{k U_2}{\alpha^2 \omega_0 L_0}, & I_{f2} &= \frac{k U_1}{\alpha^2 \omega_0 L_0}. \end{aligned} \quad (22)$$

Thus, the output power is

$$P_{\text{out}} = U_2 I_{f2} = \frac{k U_1 U_2}{\alpha^2 \omega_0 L_0}. \quad (23)$$

The charging current is also proportional to the inverter DC voltage, making it a constant-current output characteristic.

### 3.2 Model based on DEs

Similarly, only consider the first half cycle.  $t_0$  is the zero crossing point of  $i_{f2}$ , where  $U_2$  changes from negative to positive. During the stage  $[0, t_0]$ ,  $S_1, S_4, D_2$ , and  $D_3$  are on and the other switches are off; during the stage  $[t_0, T/2]$ ,  $S_1, S_4, D_1$ , and  $D_4$  are on and the other switches are off.

Take the inductor currents and capacitor voltages  $i_1, i_2, i_{f1}, i_{f2}, u_{C1}, u_{C2}, u_{Cf1}$ , and  $u_{Cf2}$  as the state variables, and the model in Fig. 4 for the stage  $[0, t_0]$  can be established by

$$\begin{cases} U_{\text{inv}} = L_{f0} \frac{di_{f1}}{dt} + u_{Cf1}, & U_{\text{rec}} = L_{f0} \frac{di_{f2}}{dt} + u_{Cf2} \\ u_{Cf1} = u_{C1} + L_0 \frac{di_1}{dt} + k L_0 \frac{di_2}{dt}, & i_1 = C_0 \frac{du_{C1}}{dt} \\ u_{Cf2} = u_{C2} + L_0 \frac{di_2}{dt} + k L_0 \frac{di_1}{dt}, & i_2 = C_0 \frac{du_{C2}}{dt} \\ i_{f1} = C_{f0} \frac{du_{Cf1}}{dt} + i_1, & i_{f2} = C_{f0} \frac{du_{Cf2}}{dt} + i_2 \end{cases}. \quad (24)$$

The DEs for the coil currents can be derived as

$$\begin{cases} \frac{1+k}{\omega_0^4(1-\alpha)} \frac{d^4(i_1+i_2)}{dt^4} + \frac{2+k}{\omega_0^2(1-\alpha)} \frac{d^2(i_1+i_2)}{dt^2} + (i_1+i_2) = 0 \\ \frac{1-k}{\omega_0^4(1-\alpha)} \frac{d^4(i_1-i_2)}{dt^4} + \frac{2-k}{\omega_0^2(1-\alpha)} \frac{d^2(i_1-i_2)}{dt^2} + (i_1-i_2) = 0 \end{cases}. \quad (25)$$

There are eight characteristic roots for the two DEs in (25), expressed as

$$\lambda_{1,2} = \pm j\omega_0 \sqrt{\frac{(2+k) - \sqrt{k^2 + 4\alpha(1+k)}}{2(1+k)}}, \quad (26)$$

$$\lambda_{3,4} = \pm j\omega_0 \sqrt{\frac{(2+k) + \sqrt{k^2 + 4\alpha(1+k)}}{2(1+k)}}, \quad (27)$$

$$\lambda_{5,6} = \pm j\omega_0 \sqrt{\frac{(2-k) - \sqrt{k^2 + 4\alpha(1-k)}}{2(1-k)}}, \quad (28)$$

$$\lambda_{7,8} = \pm j\omega_0 \sqrt{\frac{(2-k) + \sqrt{k^2 + 4\alpha(1-k)}}{2(1-k)}}. \quad (29)$$

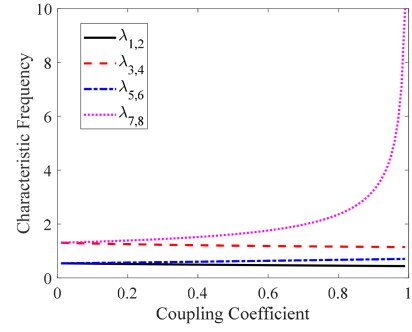


Fig. 5 Characteristic frequencies varying with the coupling coefficient of the LCC–LCC compensation

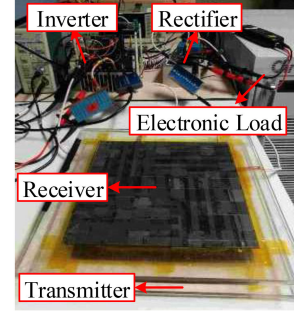


Fig. 6 Photograph of experimental prototype with the SS compensation

When  $\alpha=0.5$ , the four characteristic angular frequencies, which are the imaginary parts of (26)–(29), changing with the coupling coefficient  $k$  are plotted in Fig. 5. We can see that the characteristic root  $\lambda_{7,8}$  is the largest. When  $k$  is close to 1, it can be simplified as

$$\lambda_{7,8} = \frac{\pm i\omega_0}{\sqrt{1-k}}. \quad (30)$$

When  $k=0.889$ , this largest root triples  $\omega_0$ . Since the square wave of the inverter AC voltage has a large third harmonic component, the WPT system with the LCC–LCC compensation at this particular coupling coefficient will have a large third harmonic current, leading to a low efficiency and the failure of FHA to describe the WPT system.

## 4 Calculations and experiments

### 4.1 SS compensation

An experimental prototype of the WPT system with the SS compensation is implemented, as shown in Fig. 6. The inductances change with the coupling. With a stronger coupling, the coil is closer to the ferrite on the other side, leading to larger inductances. Three cases of couplings are studied. Case 1: when  $k=0.80$ ,  $L_0=62.5 \mu\text{H}$ ,  $C_0=62 \text{ nF}$ , and  $f_0=81 \text{ kHz}$ ; Case 2: when  $k=0.89$ ,  $L_0=72 \mu\text{H}$ ,  $C_0=54.8 \text{ nF}$ , and  $f_0=80 \text{ kHz}$ ; Case 3: when  $k=0.92$ ,  $L_0=78 \mu\text{H}$ ,  $C_0=54.8 \text{ nF}$ , and  $f_0=77 \text{ kHz}$ .

For Case 1,  $U_{\text{rec}}$  is set to 100 V. By varying  $U_{\text{inv}}$ , the RMS values of  $I_1$  and  $I_2$  of Case 1 are shown in Fig. 7. With a strong coupling, the proposed model matches the experimental results better than FHA. The RMS values calculated by FHA are smaller due to the ignorance of the harmonics.

When  $U_{\text{inv}}=200 \text{ V}$  and  $U_{\text{rec}}=100 \text{ V}$ , the voltage and current waveforms are depicted in Fig. 8. The model based on DEs matches the experiments well in all cases. With a strong coupling, the transmitter and receiver currents are distorted and FHA is no longer effective; with a weak coupling, the currents are approximately sinusoidal and FHA may be applicable. In this case, by doing fast Fourier transform to the transmitter and receiver current, it is found that the major harmonics are the third and fifth harmonics, as shown in Fig. 9. The composition of the first, third, and fifth harmonics resembles the original waveforms. There are

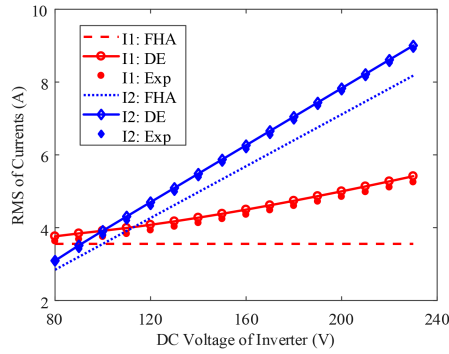


**Fig. 7** RMS values of transmitter and receiver currents of the SS compensation at 0.80 coupling coefficient

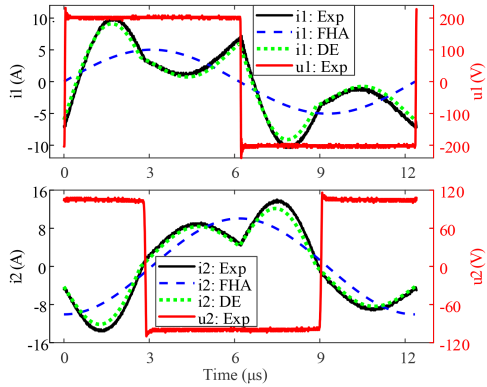


**Fig. 8** Voltage and current waveforms of the SS compensation when  $k = 0.80$

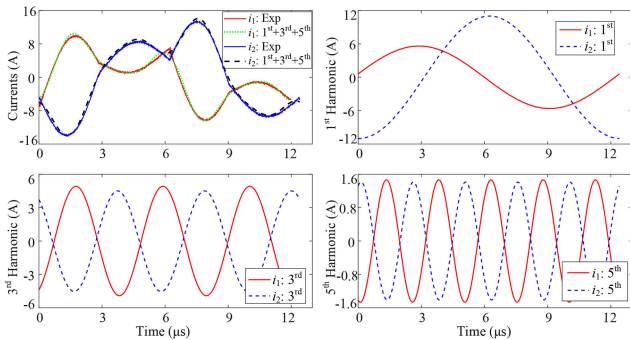


**Fig. 9** Decomposition of transmitter and receiver currents of the SS compensation when  $k = 0.80$

large amounts of third and fifth harmonics in both the transmitter and receiver currents. The third harmonic of the transmitter current has approximately the same amplitude as that of the receiver current, so is the fifth harmonic. When the phase difference between the transmitter and receiver currents is zero or close to zero, hardly any power will be transferred via the currents. Therefore, the power is only transferred via the fundamental harmonic and no power is transferred via the third or the fifth harmonics. The third and the fifth harmonics only contribute to losses.

For Case 1, when  $k = 0.80$ ,  $U_{rec}$  is set to be 200 V and  $U_{inv}$  is changed for target power levels under different operating frequencies. The experimental results of  $I_1$  and  $I_2$ ,  $U_{inv}$ , and the DC–DC efficiency varying with the operating frequency are depicted in Fig. 10. Based on (4), the two characteristic frequencies in this case are  $0.75f_0$  and  $2.21f_0$ . As can be seen from Fig. 10, the WPT system has a constant-voltage output at the two characteristic frequencies. The DC–DC efficiency at the left side of the resonant frequency is smaller than that at the right side.

When the operating frequency is 1.3 times the resonant frequency, the waveforms based on DEs and the experimental

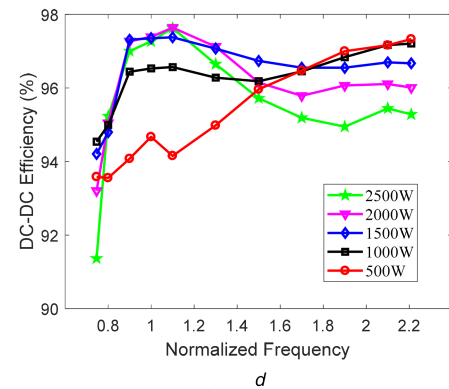
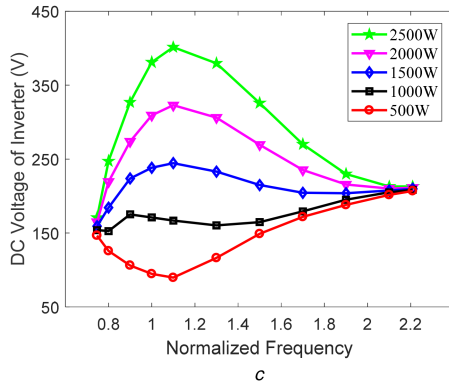
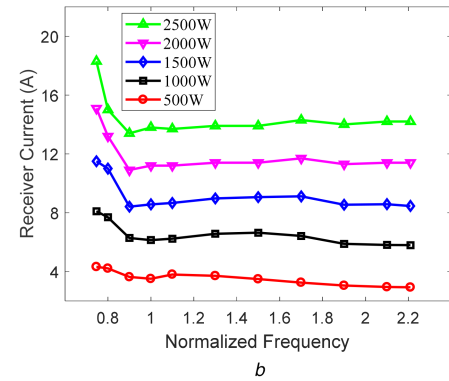
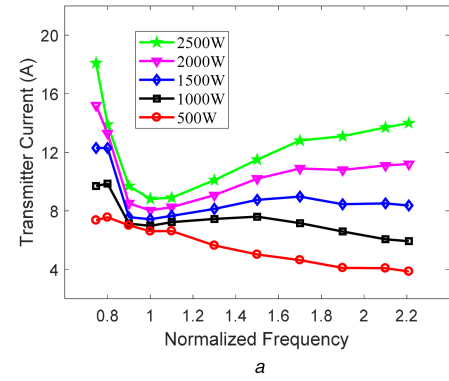


**Fig. 10** Experimental results of the SS compensation varying with the operating frequency when  $k = 0.80$

(a) Transmitter current, (b) Receiver current, (c) Required inverter DC voltage, (d) DC–DC efficiency

waveforms are shown in Fig. 11. The proposed model matches the measurements even off the resonant frequency.

For Case 2 and Case 3, the experimental waveforms when  $U_{inv} = 200$  V and  $U_{rec} = 100$  V are shown in Fig. 12. We can see that the receiver currents of these two cases are discontinuous. For Case 2 where  $k = 0.89$ , there are large third harmonic components in the currents, as expected in Section 2. In this discontinuous mode, there are more stages other than two as stated in Section 2.

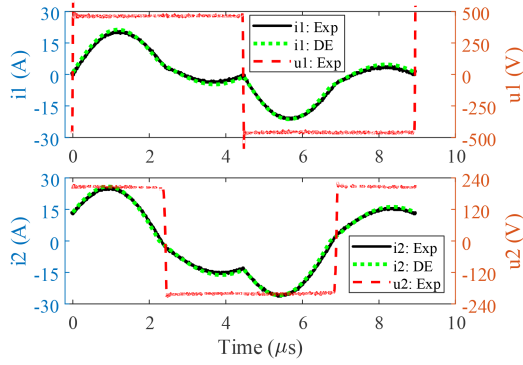


**Fig. 11** Voltage and current waveforms of the SS compensation off the resonant frequency when  $k = 0.80$

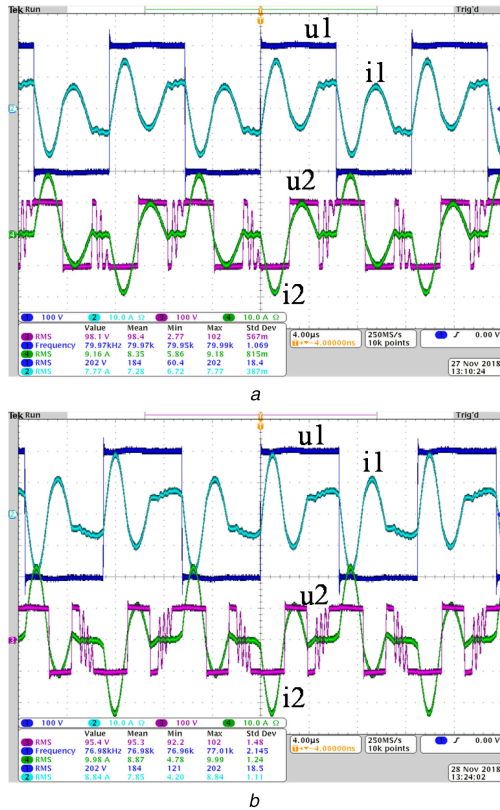


**Fig. 12** Experimental waveforms of the SS compensation (a) Case 2, (b) Case 3

However, a similar process can be performed to study the characteristics.

For the three cases,  $U_{rec}$  is set to 100 V and  $U_{inv}$  is varied. The experimental results of the DC–DC efficiency and the output power are shown in Fig. 13. We can see that the DC–DC efficiency of Case 1 is the highest, while for Case 2 and Case 3, the DC–DC efficiency decreases, even though they have larger coupling coefficients. For the output power, the trend that a larger coupling coefficient leads to a smaller output power is still effective. However, the waveform distortion leads to the inaccuracy of FHA. With a small  $U_{inv}$ , the output power of Case 2 and Case 3 is approximately the same.

#### 4.2 LCC–LCC compensation

A different coil set is developed for the LCC–LCC compensation, as shown in Fig. 14. The reason for using another coil set is that to output a few kilowatts under certain DC voltages of the inverter and the rectifier, the required inductances for the SS and LCC–LCC compensations are different. Three cases are studied: (1)  $k = 0.80$ ,  $L_1 = L_2 = 365 \mu\text{H}$  and  $\alpha = 0.523$ ; (2)  $k = 0.89$ ,  $L_1 = L_2 = 453 \mu\text{H}$  and  $\alpha = 0.578$ ; (3)  $k = 0.93$ ,  $L_1 = L_2 = 520 \mu\text{H}$  and  $\alpha = 0.633$ .

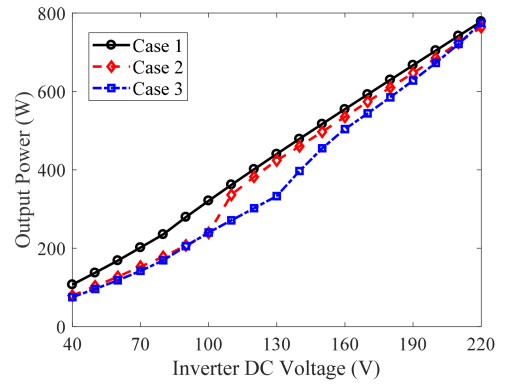
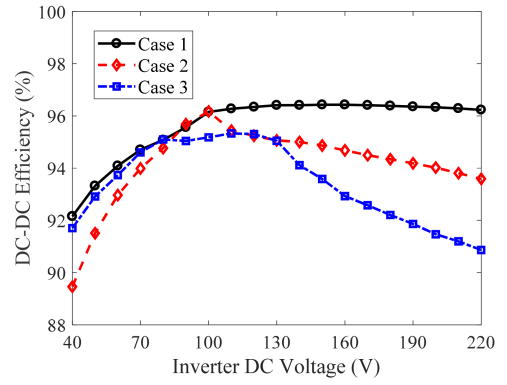


**Fig. 13** Experimental results of the SS compensation (a) DC–DC efficiency, (b) Output power

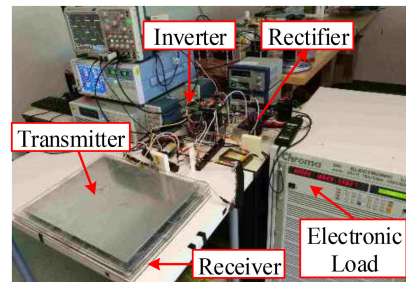


**Fig. 14** Photograph of experimental prototype with the LCC–LCC compensation

The calculations based on FHA and the experimental results of the transmission coil currents and compensation coil currents are plotted in Fig. 15. For  $k = 0.80$  and  $0.93$ , the calculations based on FHA agree well with the experimental results. Because  $U_{rec}$  is fixed,  $I_{T1}$  and  $I_2$  are constant, and  $I_1$  and  $I_{T2}$  increase with the increasing  $U_{inv}$ . For  $k = 0.89$ , the calculations of the compensation coil currents agree well with the experimental results, but the calculations of the transmission coil currents are much smaller than the experimental results.  $I_2$  is no longer constant. The reason for these discrepancies is that at this specific coupling coefficient ( $k = 0.89$ ), the third-order harmonics of the transmission coil currents are amplified, as shown in Fig. 16. For the cases with other coupling coefficients, the current waveforms can be regarded to be sinusoidal. Thus, FHA is still applicable.

The calculations and the experimental results of the output power and the measured DC–DC efficiency are depicted in Fig. 17. Due to the fact that the calculations of the compensation coil currents are consistent with the experimental results, the calculated output power matches the experimental results well. Since large third harmonic currents are generated in the transmission coil currents which leads to a large loss, the efficiency of the case with the coupling coefficient of  $0.89$  is smaller than those of other coupling coefficients with an efficiency drop of over 3%, which is crucial especially for high-power systems. Therefore, when

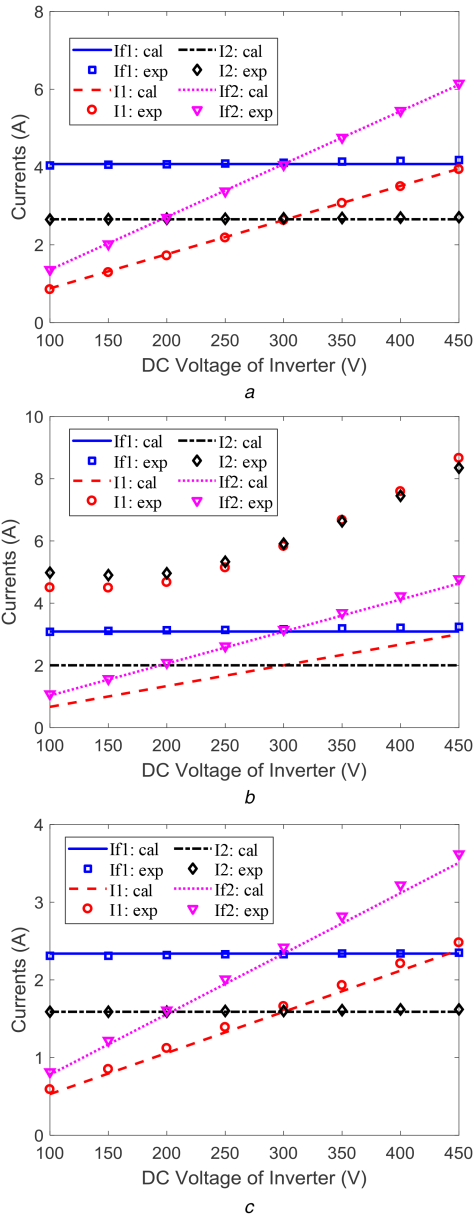


**Fig. 15** Calculations and experimental results of transmission coil currents and compensation coil currents of the LCC-LCC compensation (a)  $k=0.80$ , (b)  $k=0.89$ , (c)  $k=0.93$

designing a strongly-coupled WPT system with the LCC-LCC compensation, the coupling coefficient around 0.889 should be avoided.

### 4.3 Comparison

Comparing the SS and LCC-LCC compensations, we can find that the SS compensation has high distortions when the coupling coefficient is strong enough, typically over 0.7; while the LCC-LCC compensation only has high distortions with large third-order harmonics when the coupling coefficient is around 0.889. Distortions lead to larger current RMS values and lower efficiency. Thus, the LCC-LCC compensation is a more suitable topology for strongly-coupled WPT systems considering distortions.

## 5 Conclusion

This paper conducted the modelling and analysis of strongly coupled WPT systems with the SS and LCC-LCC compensations exhibiting distortions. The models of the SS and LCC compensations were established based on the DEs. It was found that two sinusoidal components with different frequencies coexist in the transmitter and receiver currents in the SS compensation and

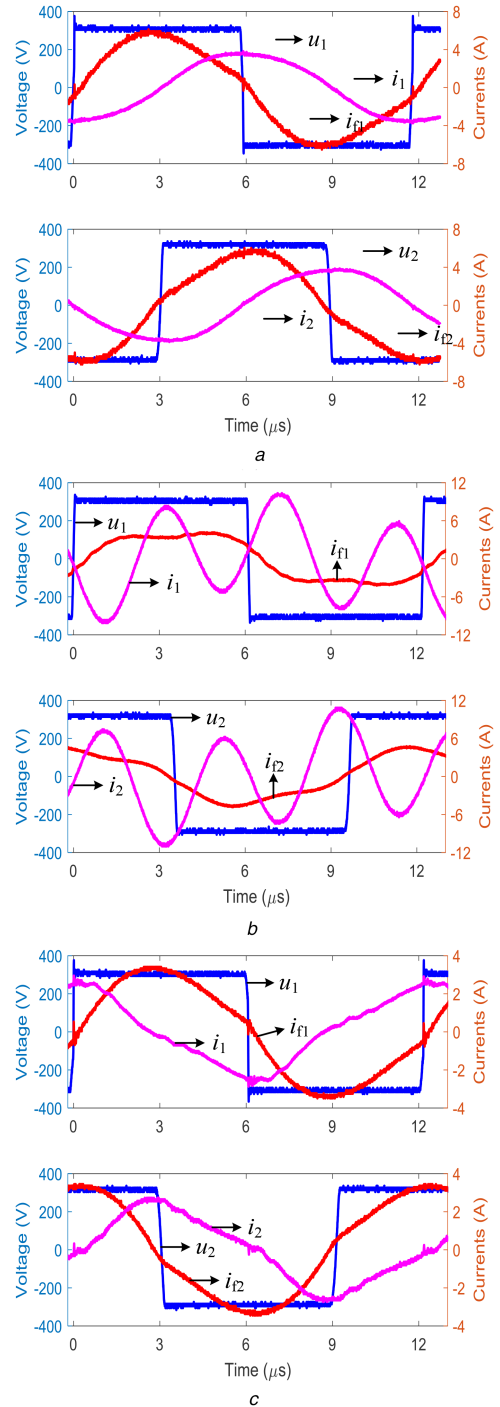


**Fig. 16** Experimental waveforms of transmission coil currents and compensation coil currents of the LCC-LCC compensation (a)  $k=0.80$ , (b)  $k=0.89$ , (c)  $k=0.93$

they are significantly different with a strong coupling, leading to the current distortion. In this case, FHA offers inaccurate results with smaller current RMS values than the measurements, which affects the selection of the power switches and the resonant capacitors. The distorted current waveforms are mainly composed of the fundamental, the third, and the fifth harmonics. The third and fifth harmonics make little contribution to the power transfer but cause additional losses in the coils. For the LCC-LCC compensations with a strong coupling, the coil currents remain sinusoidal except at the vicinity of 0.889 coupling coefficient. A large third-order harmonic current is generated in the transmission coil currents, which leads to a significant efficiency drop of over 3% and much larger current RMS ratings than estimated by FHA. Therefore, the operation zone around the coupling coefficient of 0.889 should be avoided for the LCC-LCC compensations.

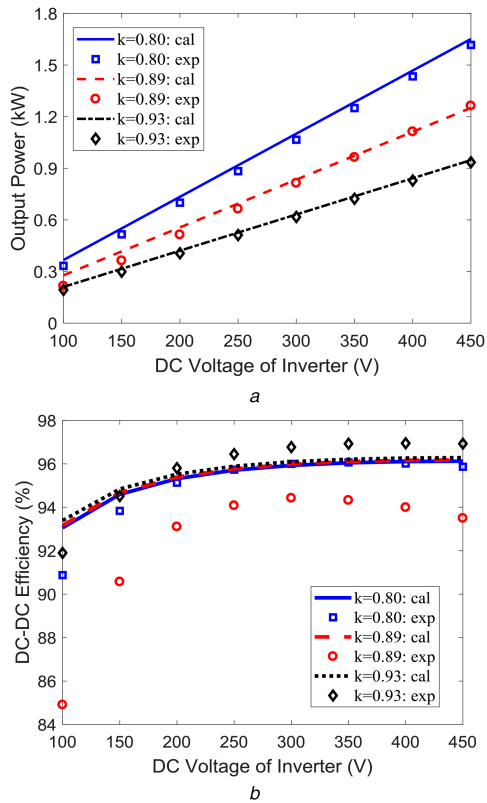


**Fig. 17** Experimental results varying with the inverter DC voltage of the LCC-LCC compensation  
(a) Output power, (b) DC-DC efficiency

Experimental prototypes were implemented and the experimental results validated the effectiveness of the proposed models.

The proposed models are helpful in understanding the mechanism of the current distortion and practical design of WPT systems with a strong coupling, such as the selection of power electronics switches and compensation capacitors, since distortions lead to much larger current ratings than the estimations by FHA. Studies in this paper show that considering the distortion, the LCC-LCC compensation is a more suitable topology for a strongly-coupled WPT system, if the coupling near the vicinity of 0.889 can be avoided.

## 6 Acknowledgments

The authors thank Huawei Technologies Co., Ltd for the support of this paper under grant no. 9406139.

## 7 References

- [1] Zhong, W.X., Liu, X., Hui, S.Y.R.: 'A novel single-layer winding array and receiver coil structure for contactless battery charging systems with free-positioning and localized charging features', *IEEE Trans. Ind. Electron.*, 2011, **58**, (9), pp. 4136-4144
- [2] Knecht, O., Kolar, J.W.: 'Comparative evaluation of IPT resonant circuit topologies for wireless power supplies of implantable mechanical circulatory support systems'. Proc. IEEE APEC, Tampa, FL, USA, 2017, pp. 3271-3278
- [3] Kan, T., Nguyen, T., White, J.C., et al.: 'A New integration method for an electric vehicle wireless charging system using LCC compensation topology: analysis and design', *IEEE Trans. Power Electron.*, 2017, **32**, (2), pp. 1638-1650
- [4] Kim, J.H., Lee, B., Lee, J., et al.: 'Development of 1-MW inductive power transfer system for a high-speed train', *IEEE Trans. Ind. Electron.*, 2015, **62**, (10), pp. 6242-6250
- [5] Huang, S., Li, Z., Lu, K.: 'Frequency splitting suppression method for four-coil wireless power transfer system', *IET Power Electron.*, 2016, **9**, (15), pp. 2859-2864
- [6] Yang, Q., Lin, B., Luan, Y., et al.: 'Distributed capacitance effects on the transmission performance of contactless power transfer for rotary ultrasonic grinding', *IET Power Electron.*, 2018, **11**, (3), pp. 548-556
- [7] Li, Z., Zhu, C., Jiang, J., et al.: 'A 3-kW wireless power transfer system for sightseeing Car supercapacitor charge', *IEEE Trans. Power Electron.*, 2017, **32**, (5), pp. 3301-3316
- [8] Ye, Z., Sun, Y., Dai, X., et al.: 'Energy efficiency analysis of U-coil wireless power transfer system', *IEEE Trans. Power Electron.*, 2016, **31**, (7), pp. 4809-4817
- [9] Huang, S.D., Li, Z.Q., Lu, K.Y.: 'Transfer efficiency analysis of wireless power transfer system under frequency drift', *J. Appl. Phys.*, 2015, **117**, (17), pp. 17E-706E
- [10] Yin, N., Xu, G., Yang, Q., et al.: 'Analysis of wireless energy transmission for implantable device based on coupled magnetic resonance', *IEEE Trans. Magn.*, 2012, **48**, (2), pp. 723-726
- [11] Luo, B., Wu, S., Zhou, N.: 'Flexible design method for multi-repeater wireless power transfer system based on coupled resonator bandpass filter model', *IEEE Trans. Circuits Syst. I, Regul. Pap.*, 2014, **61**, (11), pp. 3288-3297
- [12] Koh, K.E., Beh, T.C., Imura, T., et al.: 'Novel band-pass filter model for multi-receiver wireless power transfer via magnetic resonance coupling and power division'. Proc. IEEE Annual Wireless Microw. Tech. Conf., Cocoa Beach, FL, USA, 2012, pp. 1-6
- [13] Zhang, Y., Lu, T., Zhao, Z., et al.: 'Employing load coils for multiple loads of resonant wireless power transfer', *IEEE Trans. Power Electron.*, 2015, **30**, (11), pp. 6174-6181
- [14] Fu, M., Zhang, T., Ma, C., et al.: 'Efficiency and optimal loads analysis for multiple-receiver wireless power transfer systems', *IEEE Trans. Microw. Theory Tech.*, 2015, **63**, (3), pp. 801-812
- [15] Zhang, Y., Zhao, Z., Chen, K.: 'Load matching analysis of magnetically-coupled resonant wireless power transfer', *Proc. IEEE ECCE Asia*, Melbourne, USA, 2013, pp. 788-792
- [16] Bi, Z., Kan, T., Mi, C.C., et al.: 'A review of wireless power transfer for electric vehicles: prospects to enhance sustainable mobility', *Appl. Energy*, 2016, **179**, pp. 413-425
- [17] Safaee, A., Woronowicz, K.: 'Time-Domain analysis of voltage-driven series-series compensated inductive power transfer topology', *IEEE Trans. Power Electron.*, 2017, **32**, (7), pp. 4981-5003
- [18] Deng, J., Pang, B., Shi, W.: 'A new integration method with minimized extra coupling effects using inductor and capacitor series-parallel compensation for wireless EV charger', *Appl. Energy*, 2017, **207**, pp. 405-416
- [19] Zhang, W., Wong, S., Tse, C.K.: 'Load-Independent duality of current and voltage outputs of a series- or parallel-compensated inductive power transfer converter with optimized efficiency', *IEEE J. Emerg. Sel. Top. Power Electron.*, 2015, **3**, (1), pp. 137-146